Optics Letters

Sub-megahertz linewidth 780.24 nm distributed feedback laser for ^{87}Rb applications

E. Di Gaetano,* S. Watson, E. McBrearty, M. Sorel, and D. J. Paul

University of Glasgow, James Watt School of Engineering, Rankine Building, Oakfield Avenue, Glasgow, G12 8LT, United Kingdom
**Corresponding author: Eugenio. DiGaetano@glasgow.ac.uk*

Received 2 April 2020; revised 22 May 2020; accepted 25 May 2020; posted 26 May 2020 (Doc. ID 394185); published 24 June 2020

A distributed feedback GaAs-based semiconductor laser with a laterally coupled grating is demonstrated at a wavelength of 780.24 nm with up to 60 mW power. A mode expander and aluminum-free active layers have been used to reduce the linewidth to 612 kHz while maintaining high output power. The laser demonstrates over 40 dB side-mode suppression ratio with >0.3 nm of tuning suitable for atom cooling experiments with the D2 ^{87}Rb atomic transition. This laser has substantial potential to be integrated into miniaturized cold atom systems.

https://doi.org/10.1364/OL.394185

Emerging technologies based on cold atoms such as atomic clocks [1,2] rely on accurate measurements through locking a laser to a stable atomic transition. These high-accuracy devices, however, require stringent laser properties in terms of linewidth, stability, and power output; therefore, the laser systems are typically bulky, expensive, and power-hungry [1,2]. Semiconductor lasers offer good chip-scale integrability [3–5], low production cost, and reduced power consumption [6], which are all desirable properties for the realization of compact clock systems [7]. Of particular relevance is the GaAs/AlGaAs material platform because it can cover a wide wavelength emission range from 700 nm to 900 nm, which includes important cold atom transition lines such as ^{87}Rb and ^{133}Cs at 780.24 nm and 852 nm, respectively [8].

One of the critical issues for the development of high-power lasers on a GaAs/AlGaAs material platform is the aluminum-oxide formation on the air-exposed surfaces. Not only does such oxide formation decrease the power density threshold for catastrophic optical damage (COD) and mirror damage (COMD) [9,10], but it also degrades the laser output in terms of carrier lifetime, propagation losses, and self-heating [11–13]. Moreover, the aluminum fraction in the epilayer material poses several issues for epitaxially regrown structures where the oxygen contamination of the aluminum-containing layers can substantially decrease the fabrication yield. One of the possible solutions to mitigate the aluminum oxidation is the use of an aluminum-free active area [14]. From an optical gain point of view, the majority of the structures reported in the literature are designed with a large overlap between the optical mode and the gain region to minimize the laser threshold. Such design strategy is, however, not ideal for high-power and narrow-linewidth lasers as structures with low power density and low internal losses are desirable to both extend the power range with single-mode operation and reduce the linewidth in accordance to the Schawlow–Townes formula [15].

In this work, a distributed feedback (DFB) laser design is proposed to reduce the linewidth at the emission wavelength of 780.24 nm. An aluminum-free active area was designed with InGaAsP quaternary layers to reduce the risk of COD and COMD. In addition, a mode expander layer was introduced in the n-doped AlGaAs cladding to stretch the optical mode vertically, thereby decreasing the average power density and the internal propagation losses. Finally, a long cavity of 4 mm was employed to further decrease the average power density and reduce the laser linewidth. The fabricated DFB lasers exhibited stable emission wavelength of 780.24 nm with powers up to 60 mW and linewidths down to 612 kHz, a value suitable for the ^{87}Rb atom cooling at the D2 transition (<1 MHz [16]).

The first aspect we considered in the laser optimization was the epilayer design of the active region. In order to limit the interaction of the optical mode with the aluminum-containing layers, InGaAsP quaternary compounds were chosen for the quantum wells (QWs) and barriers, and these layers were simulated using the Schrödinger–Poisson current solver Nextnano++ [17]. Two compressively strained 4-nm-thick $In_{0.413}Ga_{0.587}As_{0.44}P_{0.56}$ QWs inserted between 10-nm-thick $In_{0.27}Ga_{0.73}As_{0.44}P_{0.56}$ barriers provide laser emission around 780.24 nm. The active area is enclosed between two graded separate confinement heterostructure (GRINSCH) layers of AlGaAs with aluminum fraction gradually increasing from 0.4 to 0.55. Finally, the GRINSCH layers are sandwiched between two doped $Al_{0.55}Ga_{0.45}As$ cladding layers. The use of an aluminum-free active area reduces the optical confinement factor of the optical mode within aluminum-containing layers by 10% in comparison to standard GaAs/AlGaAs designs [18] and gives more tolerance in defining the DFB gratings as the active area can be etched without introducing additional scattering losses or decreasing the power density threshold for COD and COMD [9,10].

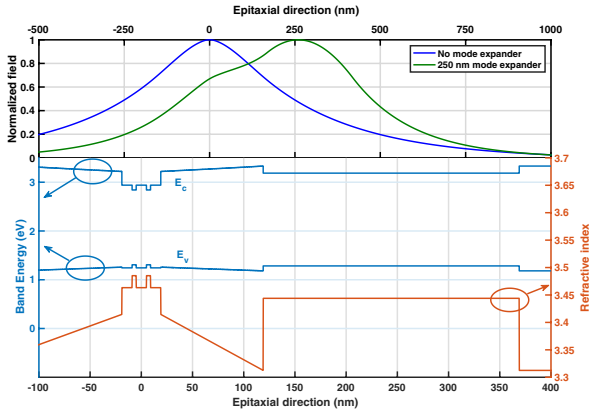

Fig. 1. Top left axis, the vertical mode profile; bottom left axis, the conduction and valence bands for the active area; bottom right axis, the refractive index for the mode expander. The zero position in the x axis represents the center of the active area.

The Schawlow–Townes formula is an effective tool to analyze the impact of the epilayer design on the laser linewidth [15]. For semiconductor DFB lasers, the formula can be expressed as

$$\Delta\nu = \Gamma_{QW}\frac{r_{sp}}{R_{sp}}\frac{h\nu(\alpha_i+\alpha_m)\alpha_m(1+\alpha_H)^2}{4\pi P_{\text{out}}}. \quad (1)$$

Equation 1 indicates that lasers with low $\Delta\nu$ require low propagation losses α_i, equivalent mirror losses for DFB lasers α_m, mode confinement in the active QW region Γ_{QW}, and Henry factor α_H. Also, linewidth narrowing can be obtained by increasing the output power P_{out} of the laser. It is worth noting that α_i and Γ_{QW} are predominantly related to the design of the gain material, while α_m depends on the grating design; hence, these contributions to the linewidth can be independently optimized. The linewidth enhancement factor α_H has a substantial impact on nonlinear effects such as spatial hole burning (SHB), and is critical for narrow-linewidth semiconductor lasers as it increases for high values of P_{out} [19], which explains the linewidth broadening experienced by high-power lasers. The other terms (i.e., $h\nu$ photon energy and r_{sp}/R_{sp} spontaneous emission fraction in the lasing mode) effecting the linewidth in Eq. (1) can be assumed as fixed terms in this treatment and will not be considered in the following.

As reported in previous work for 1550 nm lasers [20], the introduction of a mode expander layer in the n-doped cladding decreases several parameters that play a role in defining the laser linewidth in Eq. (1): (i) the mode confinement Γ_{QW}; (ii) the propagation losses α_i; and (iii) the average power density in the transversal direction $\overline{P_{\text{tran}}}$. The mode expander was implemented by introducing a layer in the lower cladding with a higher refractive index (i.e., $Al_{0.35}Ga_{0.65}As$) in comparison with the surrounding layer (i.e., $Al_{0.55}Ga_{0.45}As$), so as to pull the optical mode further into the n-doped cladding and expand the mode size. The magnitude of this effect depends on the mode expander thickness and on its distance from the active area; hence, the laser parameters Γ_{QW} and α_i can be engineered as a function of the mode expander design. The vertical mode profiles with and without the mode expander, the band structure, and the refractive index profile around the active area are reported in Fig. 1.

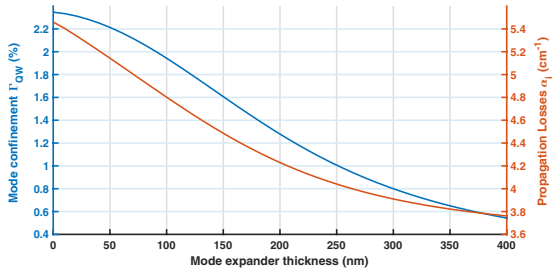

Fig. 2. Simulations of the mode confinement of the active region Γ_{QW} (left axis) and of the propagation losses α_i (right axis) as a function of the mode expander thickness for a mode expander distance of 100 nm from the edge of the active region.

The distance of the mode expander from the active area is a critical parameter because the lower energy bandgap of the mode expander layer can create an asymmetrical confinement for electrons and holes in the active area. From simulation of the energy levels and carrier confinements in the active area by Nextnano++ software, a distance between the active and the mode expander larger than 100 nm was found to be sufficient to ensure a symmetrical band structure in the active area. On the other hand, a larger distance would reduce the effect of the mode expander on the active area, which would demand a wider mode expander to achieve an equivalent mode attraction. The lower energy bandgap of the mode expander, however, acts as a potential barrier for electrons and holes; hence, it is preferable to limit the mode expander thickness to minimize the value of an additional series resistance through the epilayer. Based on these considerations, a mode expander distance of 100 nm was chosen for the epilayer design.

The fraction of the modal power overlapping with the active region Γ_{QW} and the propagation losses α_i, given by the sum of the propagation losses in the active region $\alpha_{QW}=\Gamma_{QW}k_p$, n-doped $\alpha_n=\Gamma_n k_n$, and p-doped cladding $\alpha_p=\Gamma_p k_p$ [20], are simulated through a finite difference eigenmode (FDE) 1D-simulation tool (Lumerical Mode solution [21]). The factors $k_{QW,n,p}$ represent the normalized absorption coefficients of the QWs and claddings for doping levels $n=10^{18}$ cm^{-3} and $p=6\times10^{17}$ cm^{-3}, respectively, and are obtained considering the free carrier absorption and the intervalence band absorption as the main loss mechanisms [22–24]. Both Γ_{QW} and α_i are reported in Fig. 2 as a function of the mode expander thickness.

From Eq. (1), a lower value of Γ_{QW} provides a narrower laser linewidth; however, the reduction of Γ_{QW} also effects other laser parameters such as the threshold current and the output power P_{out} [25]. Therefore, a trade-off value of 1% was selected as a design parameter as this Γ_{QW} value is sufficient to achieve a threshold current density as low as 1 kA/cm^{-2} [26] while it narrows the linewidth by a factor 2.4 in comparison to an epilayer design without the mode expander layer. For a mode expander thickness of 250 nm, which corresponds to a Γ_{QW} value of 1%, Fig. 2 also indicates a decrease of the propagation losses from α_i from 5.4 cm^{-1} to values below 4.1 cm^{-1}. This is a consequence of the larger mobility of electrons [23] compared to holes [24] in AlGaAs compounds, which translates into lower absorption in n-doped materials compared to p-doped materials. The mode expander design also has a good tolerance in terms of thickness and material composition. An inaccuracy of 10 nm in layer

thickness or 1% in aluminum fraction, which is significant compared to the tolerances for QW growths, translates in a variation of α_i and Γ_{QW} lower than 0.1 cm^{-1} and 0.1%, respectively. The decrease of α_i entails a further reduction of the linewidth according to Eq. (1). Moreover, the mode expander decreases the average power density in the transversal direction $\overline{P_{\text{tran}}}$, which is linked to the power output by the equation

$$P_{\text{out}} \propto \int_0^L (\overline{P_{\text{tran}}(L)} \times A)\mathrm{d}L, \tag{2}$$

where L is the cavity length and A is the modal cross-sectional area (i.e., defined as the area contained between the points where the field intensity decreases by a factor 1/e over the maximum). The area A depends on the transversal geometry of the waveguide, but the vertical and horizontal contributions can be considered separately as the former is mainly effected by the material epilayer and the latter is shaped by the ridge waveguide geometry. The vertical mode size d, which represents the projection of A in the vertical line including the maximum of the power intensity, is increased from 0.4 μm to 0.48 μm by the mode expander layer. As a consequence, the mode size expansion reduces the average transversal power density $\overline{P_{\text{tran}}}$ by about 20% for the same output power.

Regarding the Bragg grating design, the two key parameters to be optimized are the coupling factor κ and the cavity length L. The product κL is the total grating coupling and determines the modal gain threshold α_m in Eq. (1). It should be noted that although the grating coupling depends only on the product κL, gratings with the same values of κL but with different relative values of κ and L have different impacts on the laser properties. In fact, for the same product κL, a longer cavity translates into a lower power density and, hence, a reduction of the nonlinear effects, which could broaden the linewidth. A longer cavity, however, has higher propagation losses per round trip $\alpha_i L$, which increases the lasing threshold and decreases P_{out}; hence, its value has to be carefully optimized by considering all the laser design parameters simultaneously.

The coupling factor κ was simulated through a FDE 2D-simulator with a longitudinal approximation and confirmed through a 3D-simulator EigenMode Expansion (EME) by Lumerical MODE software for a shallow-etched sidewall Bragg grating, with a width of 1.2 μm and 2.2 μm for the two sections of the ridge waveguide, as described in a previous work [27]. The considered etching depth for the sidewall grating is 1.6 μm, which corresponds to stopping the etch 150 nm above the active area. Although the coupling coefficient κ is reduced by the effect of the mode expander layer, which pulls the optical mode out of the grating etched in the p-doped cladding, a lower value of κ is functional for achieving narrow linewidth, provided that the total grating coupling κL is above 1 [28]. In order to have the Bragg condition at the target wavelength of 780.24 nm, the grating period at the first order is ∼117 nm, which gives very low tolerances to fabrication inaccuracies. Hence, a third-order grating geometry with a 50% duty cycle and a 351 nm period was selected to relax the fabrication tolerances, providing a coupling factor of approximately 4 cm^{-1} [27], which is consistent with the coupling coefficient measured from the stop band in the DFB spectrum. The cavity length was chosen to be 4 mm, which gives a κL product of 1.6, a value optimal to ensure stable DFB lasing operation under single-mode operation [28].

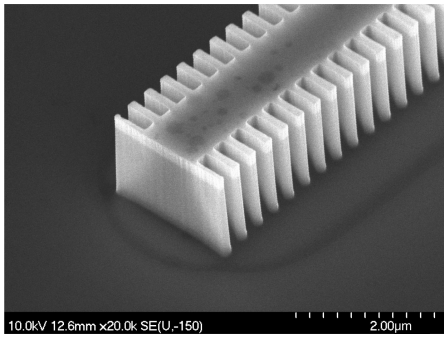

Fig. 3. A SEM picture of a sidewall DFB grating after the dry etch of the AlGaAs cladding. The high aspect ratio and sidewall smoothness prove the robustness of this critical fabrication step.

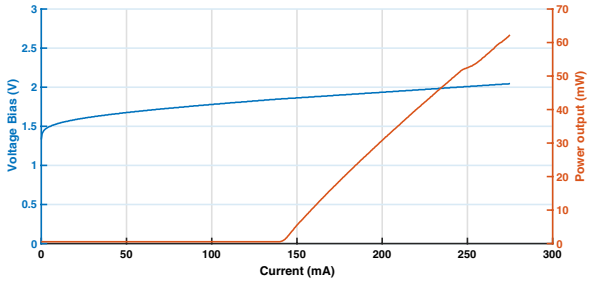

Fig. 4. The power, voltage, and current characteristics of the DFB laser.

Although a longer cavity increases the threshold current and the total propagation losses, such an increase is less prominent in lasers with a small number of QWs and low mode confinement Γ_{QW}, as for the epilayer design in this work [25]. Longer cavities are also expected to improve the thermal behavior of the laser as the dissipated heat can be spread over a longer length.

The epitaxial layers were grown by a commercial supplier on 650-μm-thick GaAs substrates. The sidewall DFB grating was patterned on a 500-nm-thick hydrogen silsesquioxane resist by electron beam lithography using a Vistec VB6 tool. The pattern was transferred to the sample by reactive ion etching using an Oxford Instrument ICP180 tool with a $Cl_2/BCl_3/Ar/N_2$ chemistry to etch through the upper cladding with a high aspect ratio, as shown in Fig. 3. The sample was then covered with a SiO_2 passivation layer, and a narrow window on the top of the waveguide was etched to allow for current injection. The top (TiPtAu) and bottom (AuGeNi) contacts were evaporated after the sample was thinned down to a thickness of approximately 250 μm. Finally, the device was cleaved before antireflection (AR) and high-reflection (HR) coatings were deposited on the cavity facets to suppress any parasitic Fabry–Perot effects.

The fabricated devices were fully characterized for light-voltage-current (LIV), optical spectrum, and linewidth characteristics under continuum-wave operation and at a fixed temperature of 20°C. The LIV characteristics shown in Fig. 4 indicate a threshold current of 140 mA with a voltage bias lower than 2 V up to an injection current of 250 mA, which demonstrates a good electrical conductivity of the epilayer. The DFB laser has kink-free emission between the threshold and an injection current of 240 mA, albeit the power output linearly increases until the injection current of 275 mA exceeds

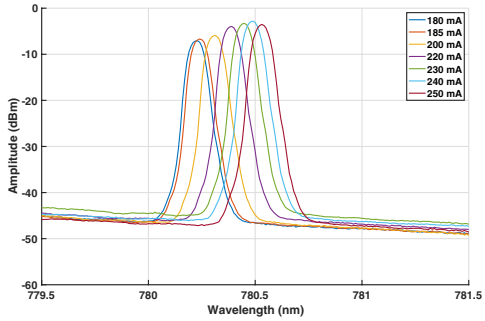

Fig. 5. The spectra of the DFB laser for different injected currents at a temperature of 20°C. The peak wavelength shows a monotonous increase with the current and can be finely tuned about the target wavelength of 780.24 nm.

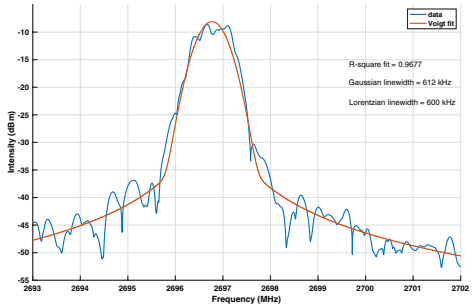

Fig. 6. RF beat signal and its Voigt fit for the narrowest linewidth obtained at the current injection of 250 mA. The FWHM is 612 kHz (single sweep with a sweep time of 25 μs; resolution bandwidth, 200 kHz; video bandwidth, 30 kHz).

60 mW. The laser spectrum was measured by an optical spectrum analyzer with 0.01 nm resolution for increasing values of the injected current in order to confirm single-mode operation and emission wavelength tuning (see Fig. 5). The DFB laser clearly exhibits single-mode behavior with no evidence of mode hopping and a side-mode suppression ratio (SMSR) exceeding 40 dB within the 180–250 mA current range and with a peak wavelength tunability of 0.3 nm.

Finally, the laser linewidth was characterized through a heterodyne detection technique [29]. The laser signal was beaten with a commercial 50 kHz Ti:sapphire laser source at 780 nm wavelength and coupled to a fast photodetector to generate a radio frequency (RF) signal. The generated RF beat note was then resolved by a RF spectrum analyzer in order to measure the full width at half-maximum (FWHM) of the convolved signals. A Voigt line shape, the convolution of a Gaussian and a Lorentzian line shape, was employed to fit the RF beat note. The natural Lorentzian-shaped laser linewidth was extrapolated from the fitted Voigt linewidth. The measured RF signal and its Voigt-shaped fit are shown in Fig. 6 with a measurement sweep time of 25 μs. The RF fitting indicates that the laser has a linewidth of 612 kHz, a value that is suitable for ^{87}Rb atomic cooling applications [16].

In conclusion, an optimized, aluminum-free active region DFB laser with a mode expander and a long-cavity laterally coupled Bragg grating has been demonstrated at 780.24 nm wavelength with a 60 mW emission. The measured SMSR of 40 dB and linewidth of 612 kHz match the requirements for ^{87}Rb D2 transitions for atom cooling applications.

Funding. Engineering and Physical Sciences Research Council (EP/M013294/1, EP/N003225/1, EP/T001046/1).

Disclosures. The authors declare no conflicts of interest.

REFERENCES

1. G. K. Campbell and W. D. Phillips, Philos. Trans. Royal Soc. A **369**, 4078 (2011).
2. A. D. Ludlow, M. M. Boyd, J. Ye, E. Peik, and P. O. Schmidt, Rev. Mod. Phys. **87**, 637 (2015).
3. K. Gallacher, M. Sinclair, R. W. Millar, O. Sharp, F. Mirando, G. Ternent, G. Mills, B. Casey, and D. J. Paul, in *Conference on Lasers and Electro-Optics* (Optical Society of America, 2019), paper STu4O.7.
4. P. Dong, T.-C. Hu, T.-Y. Liow, Y.-K. Chen, C. Xie, X. Luo, G.-Q. Lo, R. Kopf, and A. Tate, Opt. Express **22**, 26854 (2014).
5. G.-H. Duan, C. Jany, A. Le Liepvre, A. Accard, M. Lamponi, D. Make, P. Kaspar, G. Levaufre, N. Girard, F. Lelarge, J.-M. Fedeli, A. Descos, B. B. Bakir, S. Messaoudene, D. Bordel, S. Menezo, G. de Valicourt, S. Keyvaninia, G. Roelkens, D. Van Thourhout, D. J. Thomson, F. Y. Gardes, and G. T. Reed, IEEE J. Sel. Top. Quantum Electron. **20**, 158 (2014).
6. Y. Ding, G. Ternent, A. Saeed, C. J. Hamilton, N. Hempler, G. P. A. Malcolm, G. T. Maker, M. Sorel, and D. J. Paul, in *2017 European Conference on Lasers and Electro-Optics and European Quantum Electronics Conference* (Optical Society of America, 2017), pp. CB–7–2.
7. S. Knappe, P. Schwindt, V. Shah, L. Hollberg, J. Kitching, L. Liew, and J. Moreland, Opt. Express **13**, 1249 (2005).
8. J. Kitching, Appl. Phys. Rev. **5**, 031302 (2018).
9. A. Moser, Appl. Phys. Lett. **59**, 522 (1991).
10. A. Moser and E. E. Latta, J. Appl. Phys. **71**, 4848 (1992).
11. A. Knauer, H. Wenzel, G. Erbert, B. Sumpf, and M. Weyers, J. Electron. Mater. **30**, 1421 (2001).
12. M. Fukuda and G. Iwane, J. Appl. Phys. **58**, 2932 (1985).
13. P. Crump, C. Schultz, H. Wenzel, G. Erbert, and G. Tränkle, J. Phys. D Appl. Phys. **46**, 013001 (2012).
14. F.-J. Vermersch, V. Ligeret, S. Bansropun, M. Lecomte, O. Parillaud, M. Calligaro, M. Krakowski, and G. Giuliani, IEEE Photon. Technol. Lett. **20**, 1145 (2008).
15. C. Henry, IEEE J. Quantum Electron. **19**, 1391 (1983).
16. H. J. Metcalf and P. van der Straten, *Laser Cooling and Trapping* (Springer, 1999).
17. https://www.nextnano.de.
18. H. Virtanen, T. Uusitalo, M. Karjalainen, S. Ranta, J. Viheriälä, and M. Dumitrescu, IEEE Photon. Technol. Lett. **30**, 51 (2018).
19. J. Stohs, D. J. Bossert, D. J. Gallant, and S. Brueck, IEEE J. Quantum Electron. **37**, 1449 (2001).
20. L. Hou, M. Haji, J. H. Marsh, and A. C. Bryce, Opt. Express **19**, B75 (2011).
21. https://www.lumerical.com/products/mode.
22. A. Haug, Semicond. Sci. Technol. **7**, 373 (1992).
23. A. K. Saxena, Phys. Rev. B **24**, 3295 (1981).
24. D. C. Look, D. Lorance, J. Sizelove, C. Stutz, K. Evans, and D. Whitson, J. Appl. Phys. **71**, 260 (1992).
25. P. Ilroy, A. Kurobe, and Y. Uematsu, IEEE J. Quantum Electron. **21**, 1958 (1985).
26. G. Erbert, F. Bugge, A. Knauer, J. Sebastian, A. Thies, H. Wenzel, M. Weyers, and G. Trankle, IEEE J. Sel. Top. Quantum Electron. **5**, 780 (1999).
27. E. D. Gaetano and M. Sorel, Opt. Lett. **44**, 1642 (2019).
28. H. Ishii, K. Kasaya, and H. Oohashi, IEEE J. Sel. Top. Quantum Electron. **15**, 514 (2009).
29. S. Spiebberger, M. Schiemangk, A. Wicht, H. Wenzel, O. Brox, and G. Erbert, J. Light. Technol. **28**, 2611 (2010).